Programmable Viscoelasticity in Protein-RNA Condensates with Disordered Sticker-Spacer Polypeptides

Ibraheem Alshareedah[1], Mahdi Muhammad Moosa[1], Matthew Pham[2], Davit A. Potoyan[2]*, Priya R. Banerjee[1]*

[1]Department of Physics, University at Buffalo, Buffalo NY 14260, USA

[2]Department of Chemistry, Iowa State University, Ames IA 50011, USA

*All correspondence could be addressed to:

Priya R. Banerjee (email: prbanerj@buffalo.edu)

Davit A. Potoyan (email: potoyan@iastate.edu)

ABSTRACT

Liquid-liquid phase separation of multivalent proteins and RNAs drives the formation of biomolecular condensates that facilitate membrane-free compartmentalization of subcellular processes. With recent advances, it is becoming increasingly clear that biomolecular condensates are network fluids with time-dependent material properties. Here, employing microrheology with optical tweezers, we reveal molecular determinants that govern the viscoelastic behavior of condensates formed by multivalent Arg/Gly-rich sticker-spacer polypeptides and RNA. These condensates behave as Maxwell fluids with an elastically-dominant rheological response at shorter timescales and a liquid-like behavior at longer timescales. The viscous and elastic regimes of these condensates can be tuned by the polypeptide and RNA sequences as well as their mixture compositions. Our results establish a quantitative link between the sequence- and structure-encoded biomolecular interactions at the microscopic scale and the rheological properties of the resulting condensates at the mesoscale, enabling a route to systematically probe and rationally engineer biomolecular condensates with programmable mechanics.

Biomolecular condensates represent a class of dynamic membrane-less bodies that are central in compartmentalizing subcellular biochemical processes in viruses[1], bacteria[2,3], yeast[4,5], and human[6]. Past studies have reported a variety of biomolecular condensates with a broad range of physiological functions including stress response[7,8], mRNA processing[9], transcriptional activity control[10-12], and genome organization[13]. The dynamic liquid-like condensates formed by RNA-binding proteins, such as FUS, TDP43, and hnRNPA1 can further undergo a liquid-to-solid transition over time (known as maturation or aging of condensates), which can lead to pathological aggregates[7,14-16]. It is now generally accepted that the material state and dynamical properties of the protein condensates, which include viscosity, surface tension, network elasticity, and transport properties of constituent macromolecules, are key determinants of their biological functions and pathological effects inside living cells[6,17,18]. Typically, dynamic liquid-like micro-environments are deemed ideal for active regulation of biomolecular associations and modifications in a signaling event, whereas irreversible condensate maturation has been linked to neurodegenerative disorders as well as tumorigenesis[19,20]. However, identifying the physiochemical factors that determine the material properties of biomolecular condensates remains a key challenge due to the complex dynamical properties of protein-RNA condensate fluid network across different length and timescales.

A central force that drives the formation of biomolecular condensates is multivalent interactions between protein and RNA chains, leading to a liquid-liquid phase separation and/or a percolation transition[21-23]. Multivalency in a protein chain is typically encoded either by intrinsically disordered regions (IDRs) with amino acid repeat sequences (such as the Arg−Gly−Gly or RGG repeats), by folded domains (such as SH_3 and PRM modules), or a combination thereof [22]. Multivalent homotypic protein-protein and heterotypic protein-RNA interactions driving biomolecular condensation have been described by the stickers-and-spacers polymer framework [22,24-26]. For IDRs, the residues that can enable inter-chain attractive interactions include arginine (R) in R/G-rich IDRs and tyrosine (Y) in prion-like IDRs[27] and are usually reffered to as “stickers”. Additionally, the linker residues connecting these stickers are considered as “spacers”. The patterning of stickers and spacers can alter the physical properties of condensates and their phase behavior[27,28]. In theory, it is conceivable that network fluidity and stiffness can be encoded by the sequence composition and sticker identity in a polypeptide chain[29]. Hence, understanding how the sticker-spacer architecture of disordered protein chains regulates the physical properties of biomolecular condensates will be insightful for understanding biological mechanisms and designing synthetic condensates.

Several recent studies have indicated that biomolecular condensates are network fluids with variable viscoelastic properties[21,22,30-33]. The viscoelasticity is presumably a result of transient network-like structures that form via physical crosslinking among protein and/or RNA chains with finite bond lifetime[22,34]. This has led to a growing interest in utilizing suitable experimental methods to probe condensate dynamical properties across different timescales. In this study, we adopt passive microrheology with optical tweezers (pMOT) to quantify the viscoelastic properties of a series of artificial condensates formed by disordered sticker-spacer polypeptides and RNA. We find that at shorter timescales, peptide-RNA condensates have an elastically dominant rheological response, while at longer timescales, the same condensates behave as predominantly viscous liquids. The network relaxation time, viz., the timescale at which the condensate transitions from an elastically dominant behavior to a viscous behavior, is determined by the chemical identities of the stickers and spacers residues in the polypeptide chain. Using complementary biophysical assays and molecular dynamics simulations, we show that the variable viscoelastic behavior of

condensates across different polypeptide variants is strongly correlated with differences in the strength of inter-chain attractions. Accordingly, we stipulate generalizable sequence heuristics that govern the viscoelasticity of peptide-RNA condensates and connect the same to their thermodynamic phase behavior. Utilizing this acquired knowledge of sequence-phase behavior-material property relations, we test simple strategies to fine-tune the condensate viscoelasticity over multiple orders of magnitude. Similar to the polypeptides, we further show that RNA sequence and shape influence the mechanics of peptide-RNA condensates. Our findings shed light on the origin of viscoelasticity in biomolecular condensates and allude to its interconnection with fundamentally relevant physical properties such as inter-molecular attractive interactions and temperature-dependent phase behavior.

RESULTS AND DISCUSSION

Passive microrheology with optical tweezers (pMOT) offers a quantitative method for characterizing the viscoelastic properties of biomolecular condensates

Establishing a molecular grammar of sequence-encoded protein-protein and protein-RNA interactions that governs the biomolecular condensate dynamical properties requires systematic and high-resolution measurements of condensate viscoelastic properties. Direct recording of the frequency-dependent viscous and elastic moduli can provide such insights[22]. The linear viscoelastic (LVE) behavior of homotypic protein condensates has recently been studied by active oscillatory microrheology using a dual-trap optical tweezer[30,31]. However, passive non-oscillatory measurements using a single optical trap offers an attractive orthogonal route to probe the LVE properties of complex fluids due to a wide range of experimentally accessible frequencies[35,36]. Furthermore, passive microrheology with optical tweezers (pMOT) only requires a single optical trap and does not need independent calibration measurements[37-40], making it convenient and well-suited for relatively high throughput studies. Here, we employ in-droplet pMOT to map the sequence-encoded and frequency-dependent viscoelastic properties of polypeptide-RNA condensates *in vitro* over 3 decades of frequencies from a single measurement (Supplementary Note 1). Briefly, 1 µm polystyrene beads are passively embedded within a condensate (placed on a glass surface) with each condensate containing at least one probe particle (Fig. 1a). The bead is constrained within the condensate by an optical trap (Fig. 1b). The motion of the bead inside the condensate is driven by the thermal fluctuations of the medium (the condensate) and constrained by the harmonic potential of the optical trap (Fig. 1c-e). The complex modulus of the condensate can be calculated from the normalized position autocorrelation function [NPAF, $A(\tau)$] of the bead (Fig. 1f) and the trap stiffness κ as[37,39]

$$G^*(\omega) = \frac{\kappa}{6\pi a}\left(\frac{i\omega\hat{A}(\omega)}{1-i\omega\hat{A}(\omega)}\right) = G'(\omega) + iG''(\omega) \quad (1)$$

Where a is the bead radius and $\hat{A}(\omega)$ is the Fourier transform of $A(\tau)$ (see Supplementary Note 1 for further details). In equation (1), G' and G'' represent the elastic (storage) and viscous (loss) modulus of the condensate, respectively. Using pMOT, we first measured the frequency-dependent viscoelastic moduli of a model peptide-RNA condensate formed by a short disordered lysine-rich repeat polypeptide $[KGKGG]_5$ and a homopolymeric RNA $[rU]_{40}$ (rU40) (Fig. 1a). We found that $[KGKGG]_5$-rU40 condensates display a complex modulus that is dominated by the viscous component (G'') at both low and high frequencies (1 to 100 Hz), indicating a predominant liquid-like behavior (Fig. 1f&g). The zero-shear viscosity (η) of $[KGKGG]_5$-rU40 condensates,

which is directly obtained from the slope of the viscous modulus ($\eta = G'/\omega$), is ~ 0.27±0.05 Pa.s. This is ~ 300-fold higher than the viscosity of water and is nearly independent of the frequency (Fig. 1g), suggesting that these condensates behave mostly as a viscous liquid throughout the entire experimentally accessible frequency range. To cross-validate our results obtained from pMOT, we independently measured the viscosity of $[KGKGG]_5$-rU40 condensates using video particle tracking (VPT) microrheology [41] and found good agreement (Fig. 1h&i). Therefore, pMOT presents a suitable method to probe the frequency-dependent LVE properties of biomolecular condensates *in vitro* (see Supplementary Note 1).

Tunable LVE properties of peptide-RNA condensates formed by stickers-and-spacers polypeptides: A. Role of "sticker" residues

To probe how polypeptide sequence features govern the condensate viscoelastic properties, we utilized short modular multivalent polypeptides that undergo phase separation with RNAs[41-50]. The design of these peptide sequences was inspired by naturally occurring Arginine/Glycine-rich (R/G-rich) IDRs in eukaryotic ribonucleoproteins (RNPs)[51,52], which function as promiscuous RNA-binding motifs. Previous studies by our group and others have reported that Arginine in R/G-rich IDRs can be classified as "stickers" that potentiate RNP phase separation with RNA through a combination of electrostatic, cation-π and π-π interactions[44,48,53]. Due to their multivalent architecture, we hypothesized that the R/G-rich IDRs have the potential to serve as programmable stickers-and-spacers polypeptides with tunable condensation behavior in presence of RNA (Fig. 2a). To test this, we designed a synthetic repeat polypeptide encompassing 5 repeats of the RGRGG motif, $[RGRGG]_5$. pMOT experiments on $[RGRGG]_5$-rU40 condensates revealed dominant elastic behavior at high frequencies (short timescales) and viscous behavior at low frequencies (long timescales). This frequency-dependent mechanical behavior of R/G-repeat condensates is reminiscent of a typical Maxwell fluid[37] (Fig. 2b) with a single crossover frequency between the elastically dominant and predominantly viscous regimes. This crossover frequency is the inverse of the terminal relaxation time (τ_M) of the condensate network (Fig. 2b), which signifies the average peptide-RNA network reconfiguration time (or bond lifetime)[35]. For $[RGRGG]_5$-rU40 condensates, τ_M is 60±10 ms, meaning that in timescales shorter than 60 ms, the $[RGRGG]_5$-rU40 condensates behave as an elastic solid (with G'>G'') and vice-versa (Fig. 2b). This is in stark contrast with $[KGKGG]_5$-rU40 condensates which behave as a predominantly viscous liquid (Fig. 1g) within the same frequency range. Consistent with this observation, the zero-shear viscosity of R/G-rU40 condensates is ~ 4±1 Pa.s (Fig. S1), which is ~ 15-fold higher than the same for K/G-rU40 condensates. This difference in viscosity between R/G and K/G condensates is consistent with previously published reports[28,44,45,48] and signifies that the dynamical properties of these condensates can vary based on the choice of stickers (*i.e.,* Arg *vs.* Lys).

Besides Arg and Gly residues, R/G-rich domains in natural RNPs frequently contain aromatic and polar residues[49]. Our bioinformatics analysis of RG/RGG motifs from > 400 human RNA-binding proteins[54] reveal that R/G-rich IDRs are primarily interspersed with four uncharged amino acids: Tyrosine (Y), Phenylalanine (F), Serine (S), and/ or Proline (P) (Fig. 2c). The occurrence of these four residues within R/G-rich IDRs can be important for modulating self-interactions and interactions with RNA and/ or solvent-mediated interactions. As such, these sequence variations may control the material properties of polypeptide-RNA condensates. To test this idea systematically, we designed a variable sticker-spacer polypeptide sequence, $[RG\underline{X}GG]_5$, where the amino-acid $\underline{X}$ can be Y, F, S, P, or simply R (Table S1). In the context of our work,

amino acids, such as Arg or Lys that primarily contribute to the RNA binding are defined as stickers, while spacers are linker residues connecting the stickers, such as Gly. Employing our pMOT experiments on condensates formed by [RGXGG]$_5$ and rU40 RNA (Fig. S2), we found a rich variation in the viscoelastic behavior that spans two orders of magnitude depending on the identity of the amino acid X. In discussing these results, we choose [RGRGG]$_5$ as our reference system (X = Arg). Setting X = Phe, we observed a 2-fold increase in the terminal relaxation time from 60±10 ms to 110±40 ms, and ~2-fold increase in the zero-shear viscosity of peptide-rU40 condensates (Fig. 2d-f). Intriguingly, setting X = Tyr resulted in condensates that exhibited an order of magnitude increase in both the terminal relaxation time (~ 900±400 ms; Fig. 2d&e) and the zero-shear viscosity (~ 40±10 Pa.s; Figs. 2e&f & Fig. S3). The high terminal relaxation time for [RGYGG]$_5$-rU40 condensates ($\tau_M \sim 0.9$ s) indicates that these condensates are dominantly elastic over a much longer timescale than [RGRGG]$_5$-rU40 and [RGFGG]$_5$-rU40 condensates (Fig. 2g). We note that, in the context of known biological assemblies, the observed LVE behavior of [RGYGG]$_5$-rU40 condensate is comparable to that of the reconstituted extracellular matrix[55]. Consistent with these results, video particle tracking microrheology using free polystyrene beads[41] (without optical traps) revealed two clear diffusion modes for [RGYGG]$_5$-rU40 condensates, representing distinguishable elastic and viscous regimes (Fig. S4). The first mode at shorter timescales displayed a near-constant MSD as a function of time, whereas a transition to a linear diffusion ($MSD = 4D\tau^{\alpha}$; $\alpha \sim 1$) was observed at ~1200 ms. This is comparable to the terminal relaxation time obtained from pMOT (900±400 ms; Fig. S4). At the same time, the MSD obtained from [RGRGG]$_5$-rU40 condensates did not show a flat regime above 100 ms (the shortest lag time in the MSD for this sample), indicating mostly viscous behavior. This is consistent with results obtained from the pMOT assay (Fig. S4) since the terminal relaxation time of [RGRGG]$_5$-rU40 condensates is ~60 ms, beyond which the viscous modulus dominates the rheological behavior (Fig. 2e).

Contrary to X = Tyr or Phe, setting X = Pro or Ser resulted in a complete loss of elasticity across the tested frequencies (Fig. 2d) akin to the [KGKGG]$_5$-rU40 condensates. The zero-shear viscosity of [RGPGG]$_5$-rU40 condensates was ~0.19±0.08 Pa.s, which is ~ 20-fold lower than the [RGRGG]$_5$-rU40 condensates (Fig. 2f) and ~200 fold lower than the [RGYGG]$_5$-rU40 condensates. Similarly, the viscosity of [RGSGG]$_5$-rU40 condensates was found to be 0.42± 0.06 Pa.s. Taken together, our rheological measurements reveal that tyrosine, phenylalanine, and arginine are promoters of elasticity in R/G-repeat polypeptide-RNA condensates, while lysine, proline, and serine residues promote the formation of predominantly viscous condensates (Fig. 2g; Fig. S3; Table S2).

We next asked whether the observed alterations in the LVE properties of peptide-RNA condensates are reflected in biomolecular diffusion within condensates. To assess that, we measured molecular mobility of a fluorescently-labeled RNA client, rU10 using fluorescence recovery after photobleaching (FRAP). We found that the rate of fluorescence recovery of the client RNA within [RGPGG]$_5$-rU40 condensates ($t_{1/2}$=4 s) was significantly higher than that of [RGRGG]$_5$-rU40 ($t_{1/2}$=23 s), whereas [RGYGG]$_5$-rU40 condensates displayed lowest recovery rate ($t_{1/2}$=74 s; Fig. S5). The rank order of RNA mobility therefore follows the same order as the dynamical properties of these condensates (Fig. S5), providing further evidence that these condensates have tunable material properties as the “stickers” in the polypeptide chain are varied. To further characterize the physical properties of condensates as a function of polypeptide repeat sequence, we utilized a variable-size dextran recruitment assay[56,57] and measured the average mesh size of the most and least dynamic condensates (*i.e.*, [RGPGG]$_5$-rU40 and [RGYGG]$_5$-rU40

condensates, respectively). We observed that the apparent mesh size of $[RGPGG]_5$-rU40 is ~6 nm, which is 50% larger than that of $[RGYGG]_5$-rU40 (~4 nm) (Figs. S6&S7), showing a correlation with the condensate viscoelastic properties. Collectively, our results reveal that the structure and material properties of peptide-RNA condensates are governed by the choice of "RGXGG" motifs in our designed polypeptide sequences.

Tunable LVE properties of peptide-RNA condensates formed by stickers-and-spacers polypeptides: B. Role of "spacer" residues

In addition to stickers, spacer residues may also impact the condensate dynamical properties by altering the RNA-binding affinity and/or modulating the effective solvation volume of the polypeptide chain[26]. To explore such an effect, we designed a generic polypeptide $[RxRxx]_5$ where "x" represents either glycine, glutamine, alanine, proline, or leucine (G, Q, A, P, or L, respectively). We observed that G-to-P substitutions reduced the condensate viscosity by an order of magnitude (Fig. 3a-c) and resulted in at least an order of magnitude lower relaxation time (τ_M ~10 ms since the crossover is slightly beyond the experimental frequency range; Fig. 3a). However, as compared to $[RGPGG]_5$ (η~0.19±0.08 Pa.s, Fig. 2f), $[RPRPP]_5$-rU40 condensates showed a higher zero-shear viscosity (~1.3±0.2 Pa.s). This indicates that replacing arginine (i.e., "stickers") residues with proline directly impacts the peptide-RNA interactions and results in larger effects on the condensate rheological properties. For RQRQQ repeats, we also found a reduced viscosity and relatively weaker elastic component than $[RGRGG]_5$-rU40 condensates (Tables S1&S2; Fig. 3a-c). In contrast, $[RARAA]_5$-rU40 condensates showed a comparable elastic response (τ_M = 50±20 ms) and marginally higher zero-shear viscosity (~ 6±1 Pa.s) than $[RGRGG]_5$-rU40 condensates (Fig. 3). Finally, mutating G-to-L ($[RLRLL]_5$) resulted in the formation of arrested networks instead of liquid-like condensates (Fig. S8) under identical experimental conditions. These results highlight that the LVE properties of peptide-RNA condensates can independently be controlled via spacer residue variation (Fig. 3), and in combination with the stickers (Fig. 2), these alterations can further attenuate or magnify condensates' viscoelastic behavior.

The LVE properties of peptide-RNA condensates are correlated with the strength of attractive interactions between polypeptide and RNA chains

Our findings discussed above reveal sequence heuristics that encode viscoelasticity in peptide-RNA condensates. By altering the chemical identity of the stickers and spacers in disordered repeat polypeptides of the same length and similar patterning, the dynamical properties of these condensates could be varied by almost two orders of magnitude (Fig. 4a). To provide a thermodynamic basis for the observed differences in the condensate LVE properties, we consider the type and relative strength of interactions between polypeptide chains and the RNA. We and others have previously shown that the material properties of peptide-RNA condensates are governed by a combination of long-range interactions (such as attractive and/or repulsive Coulomb interactions) and short-range attractions (such as cation-π and π-π interactions)[44,48]. For cationic IDRs, arginine-rich polypeptides have higher affinity for RNA than the corresponding lysine variants due to the unique planar geometry and electronic structure of the arginine guanidino group, which allows for stronger cation-π interactions[44,48,58]. Such differences in protein-RNA interactions are reflected in the phase behavior of the mixture, revealing a significantly larger window of the phase-separated regime as a function of mixture composition for the arginine-rich polypeptide as compared to the corresponding lysine variant[44]. Therefore, the net polypeptide-RNA interaction strength is not only a critical determinant of the phase behavior, but it also

regulates the dynamical properties of the condensate network. Accordingly, we hypothesized that the peptide-RNA combinations with the most pronounced condensate viscoelastic properties are those that form the most stable condensates. To test this idea, we looked at the stability of peptide-RNA condensates against two physical parameters that control the strength of interactions in these systems: ionic strength and temperature. Increasing salt concentration decreases the electrostatic attraction between peptide and RNA chains due to the electrostatic screening by counterions. Therefore, the condensation of negatively charged RNA with positively charged peptides (such as $[RGRGG]_5$) is usually suppressed at higher salt concentrations[41-44] (Fig. S9a). The condensation behavior with temperature is rather more complex as biopolymers in solutions can undergo phase separation with an upper critical solution temperature (UCST), a lower critical solution temperature (LCST), or a combination thereof[59,60]. In our peptide-RNA system, we observed an UCST behavior (Fig. 4b). This UCST behavior suggests that inter-chain attraction drives phase separation (enthalpy-driven LLPS), and therefore, higher attractive interactions are expected to lead to a higher UCST[59,61-63]. Therefore, measuring thermo-responsive phase behavior can directly report on the relative strength of inter-molecular interactions across our various peptide-RNA mixtures.

To map the stability of condensates across a broad salt and temperature range, we used a combination of solution turbidity measurements and temperature-controlled bright-field microscopy (Fig. 4c). At room temperature (22 ±1 °C), we find that $[RGRGG]_5$-rU40 condensates remain stable up to 800 mM NaCl. For $[RGPGG]_5$-rU40 condensates, which are significantly less viscoelastic than $[RGRGG]_5$-rU40, the critical salt concentration was found to be approximately 50 mM (Fig. S9a). Intriguingly, $[RGYGG]_5$-rU40 condensates, which have stronger viscoelastic response than $[RGRGG]_5$-rU40 condensates, did not completely dissolve even at ~3000 mM NaCl (Fig. S9a). These results suggest that the net attractive interactions driving the phase separation of peptide-RNA complexes are much stronger in the case of $[RGYGG]_5$-rU40 system than $[RGRGG]_5$ and $[RGPGG]_5$ complexes with RNA. Next, we measured the phase separation temperature (T_{ph}) of selected peptide-RNA mixtures with a broad range of dynamical properties at various salt concentrations and constructed a temperature-salt state diagram. We observed that $[RGPGG]_5$-rU40 condensates dissolve at a temperature of T_{ph}=26±2 °C, while $[RGRGG]_5$-rU40 condensates have a T_{ph} > 90 °C at the same experimental buffer containing 25 mM NaCl (Fig. 4c). Increasing salt concentration to 500 mM NaCl led to a lowering of T_{ph} for $[RGRGG]_5$-rU40 condensates to 40±2 °C (Fig. 4c). Under this condition, $[RGPGG]_5$-rU40 mixture did not phase separate at all the tested temperatures (T_{ph} < 5 °C). Importantly, T_{ph} progressively increased from $[RGRGG]_5$ to $[RGFGG]_5$ to $[RGYGG]_5$ at a fixed salt concentration, thereby indicating increased strength of intermolecular interactions by P-to-R-to-F/Y substitutions (Fig. 4c). Similar to sticker variations, the substitution of G-to-P as spacers, which enhances the dynamicity of condensate network (Fig. 3), led to a significant lowering of USCT. Overall, our temperature-salt state diagram conveys two important findings, (i) The relative rank order of peptide-RNA condensate UCST provides a thermodynamic measure of net attractive interactions in the condensate network across different polypeptide variants, and (ii) the thermal and salt stability of peptide-RNA condensates and the linear viscoelastic properties are strongly correlated. In other words, peptide-RNA condensates with the most pronounced viscoelastic properties are those that are most stable against temperature and salt variation. Since condensate thermal stability is governed by the strength of intermolecular interactions that drive phase separation, we conclude

that the strength of intermolecular interactions dictates the magnitude of viscoelasticity in peptide-RNA condensates.

To explore this observed correlation further, we performed all-atom molecular dynamics simulations probing the interactions between a generic oligomer GXG and a trinucleotide rU3 RNA (UUU; Fig. 4d). The variable amino acid X was set to Pro, Arg, and Tyr. We carried out 1 μs long explicit solvent simulations with tripeptide and tri-nucleotide units packed in a cubic solvated and ionized box at ~100 mg/ml density, temperature T = 300K, salt concentration = 25 mM and pressure of 1 atmosphere using the amber 99SB-disp*-ildn force field with TIP3P model for water[64]. We extracted potentials of mean force of center of mass coordinates of residues (see Methods for simulation details). Our results show a clear and robust trend of Tyr (GYG) being the sticker residue outflanking the charged Arg (GRG) and uncharged Pro (GPG; Fig. 4e&f and Fig. S9b) in their capacity to bind to nucleotides. This is consistent with our observation that Tyr-rich peptide $[RGYGG]_5$ forms condensates that have more dominant elastic behavior than Arg-rich peptide and Pro-rich peptides ($[RGRGG]_5$ and $[RGPGG]_5$). Upon close inspection of the free energy curves (Fig. 4f), we find that Tyr forms stronger short-range π-π ring contacts with Uracil bases compared to the electrostatic and salt bridge contacts, which leads to Tyr-U bonds being longer-lived than Arg-U and Pro-U contacts (Fig. 4e). We note that similar binding free energy trend (TYR>ARG>PRO) has also been obtained through restrained simulations of single solvated amino acid and nucleobases under physiological salt conditions using different force field[65]. These differences in interaction strengths also explain the higher stability of Tyr-rich condensates against salt and temperature variation (Fig. 4c & Fig. S9a). The microscopic insights obtained from our all-atom simulations were subsequently used to carry out liquid-vapor phase coexistence simulations with the full-length peptide and RNA sequences by using coarse-grained representation of chains with 1 bead per amino acid/nucleotide [42,66]. Here we calibrate the short-range attraction of residues Pro, Arg and Tyr towards RNA (Uracil) units by tuning the short-range energy coefficient of a standard Lennard-Jones potential to match the difference in the free energy minima from the all-atom simulations. Electrostatic forces are accounted for through the standard Debye-Huckel term. Inspecting the equilibrium configurations and plotting the density profiles across the simulation box, we found that $[RGYGG]_5$-rU40 showed the strongest separation behavior with the highest molecular density in the condensed phase (Fig. 4g). This was followed by the $[RGRGG]_5$-rU40 system which also showed strong segregation albeit with a lesser density in the condensed phase than $[RGYGG]_5$-rU40 system. For $[RGPGG]_5$-rU40 mixture, phase separation was much less pronounced as evidenced by the blurred interface and a mild change in density across the condensed-dilute phase interface (Fig. 4g). These results show that by tuning intermolecular interactions, the molecular density of the condensed phase is altered. Next, we repeated the coexistence simulations at various temperature conditions and measured the molecular density in the condensed and dilute phases, which was subsequently plotted as a temperature-density phase diagram (Fig. 4h). We find that $[RGYGG]_5$-rU40 condensates show the highest stability against temperature followed by $[RGRGG]_5$-rU40 system and $[RGPGG]_5$-rU40 condensates. These results are in strong agreement with our experimental temperature-salt phase diagram (Fig. 4c). In summary, our computational analysis suggests that sequence-encoded peptide-RNA interactions lead to distinct molecular density of the condensed phase (Fig. 4g), the phase separation temperature of the system (Fig. 4h), and the bond lifetime within the condensate network (Fig. 4f), all of which are key determinants of the condensate material properties. These results also draw attention to the complex interplay of interactions (such as ionic, cation-π and π-π) that leads to emergent affinities between peptides and RNA beyond the

monomer-monomer interactions that are often used to explain biophysical properties of biomolecular condensates.

Strategies for fine-tuning the LVE properties of biomolecular condensates

Intracellular biomolecular condensates are typically multicomponent and are known to adopt a diverse range of material states from viscous fluids to viscoelastic solids[21]. These observations have inspired our search to understand the physicochemical factors that control biomolecular condensates' dynamical behavior and devise molecular-level strategies to fine-tune the same. Based on our results on binary peptide-RNA condensates (Fig. 4a), we first considered two orthogonal strategies to form condensates with adjustable viscoelasticity – (a) by sequential perturbation of sticker identity in repeat polypeptides; and (b) by mixing multiple peptides with orthogonal LVE behavior. Based on our results showing enhanced viscoelasticity of peptide-rU40 condensates upon replacing all RGRGG motifs with RGYGG motif (Fig. 2 and Fig. 4a), we considered a sequential introduction of RGYGG motifs replacing the RGRGG motifs in $[RGRGG]_5$ peptide (Fig. 5a & Table S1). This sequence perturbation strategy led to a progressive enhancement of the viscosity (~4 to ~40 Pa.s) and the terminal relaxation time (~60 to ~900 ms) of peptide-rU40 condensates as a function of the number of R-to-Y substitutions (Fig. 5b-d & Fig. S10). In our second set of experiments, instead of a single repeat polypeptide, we utilized a mixture of two polypeptides with orthogonal LVE behavior, viz., $[RGYGG]_5$, which forms predominantly elastic condensates, and $[RGPGG]_5$, which forms viscous droplets with rU40 RNA (Figs. 2d, 5e & Table S2). We observed that $[RGYGG]_5$ acts as a dopant that progressively enhances the viscoelasticity of $[RGPGG]_5$ condensates with rU40 (Fig. 5f-h). The ternary peptide-RNA mixtures ($[RGYGG]_5$, $[RGPGG]_5$, and rU40) formed homogeneous condensates at all mixing ratios with LVE properties that can be controlled by the molar ratio of $[RGYGG]_5$ and $[RGPGG]_5$ (Figs. S11&S12). We observed a monotonic increase in the zero-shear viscosity (~0.19 to ~40 Pa.s) and the terminal relaxation time (~22 to ~900 ms) as a function of $[RGYGG]_5$:$[RGPGG]_5$ ratio (Fig. 5f&g). These results suggest a plausible mechanism for the regulation of the LVE properties in multi-component biomolecular condensates, where the similarity in linear sequences promotes the formation of well-mixed condensates (as opposed to multiphasic condensates[67]) and the dissimilarity in sticker identity allows for composition-dependent regulation of the condensate viscoelasticity (Fig. 5h). Taken together, our presented results demonstrate simple design strategies to control the mechanical behavior of biomolecular condensates formed by stickers-and-spacers polypeptides (Fig. 5).

Tunable LVE properties of peptide-RNA condensates by RNA sequence and structure

So far in this study, our discussions have been focused on the role of polypeptide sequence variation on the condensate dynamical properties. Evidences are also emerging that RNA sequence composition and structure are important determinants of the physical properties and function of biomolecular condensates[68]. In the context of our designed condensates, we observed that cation-π and π-π interactions between the polypeptide and RNA nucleobases enhance condensate viscoelastic behavior (Figs. 2&4). Similar modulation of condensate material properties may be achieved with RNA primary sequence variation leveraging the unique structural differences between purine (contain 10 π-electrons) and pyrimidine (contain 6 π-electrons) bases and/or their secondary structure[69]. Previous studies by our group reported that condensates formed by R/G-rich polypeptides and homopolymeric purine-containing RNAs [poly(A)] display

substantially slower fusion speed as compared to homopolymeric pyrimidine-containing RNAs [poly(U)][44]. This was attributed to the presence of stronger short-range interactions (cation-π and π-π) between purine bases with R-rich IDRs[70]. Here we considered the possibility of altering the condensate dynamical properties by sequence patterning and secondary structure of RNA chains. To test this idea, we first used a single-stranded nucleic acid (ssNA, $G_5T_{30}C_5$) with a stem-loop structure, and compared the resultant condensate network dynamics with condensates formed by an unstructured nucleic acid dT40 (Fig. 6a&b). The dynamical properties of $[RGPGG]_5$-dT40 condensates are nearly identical to $[RGPGG]_5$-rU40 RNA with the viscous modulus G'' dominating the rheological response throughout the experimental frequency range (Fig. 6c). On the contrary, $[RGPGG]_5$-$G_5T_{30}C_5$ condensates displayed enhanced viscoelasticity with a network relaxation time of ~ 24 ± 9 ms (Fig. 6d). The viscosity of $[RGPGG]_5$-$G_5T_{30}C_5$ condensates is 1.7 ± 0.2 Pa.s, which is one order of magnitude higher than the viscosity of $[RGPGG]_5$-dT40 condensate (0.14 ± 0.03 Pa.s; Fig. 6e&f). These results showcase the effect of RNA sequence composition and secondary structure on the viscoelasticity of biomolecular condensates. We next tested another structured ssNA consisting of five GGGGCC repeats, $(G4C2)_5$, which is known to form stable G-quadruplex structure[71]. Increased numbers of the G4C2 repeats in the C9orf72 gene have been genetically associated with neurodegeneration in amyotrophic lateral sclerosis (ALS) and frontotemporal dementia (FTD) patients[72]. At the same time, G-quadruplex structure forming NAs have previously been reported to interact with R/G-rich IDRs in ribonucleoproteins[73-75]. We observed that $(G4C2)_5$ NA formed spherical condensates in the presence of $[RGPGG]_5$ (Fig. 6g) albeit the condensates did not facilitate optical trapping of embedded beads likely due to their higher refractive index (hence lower refractive index mismatch with the beads) and density. To assess their dynamical behavior, we performed video particle tracking microrheology with 200 nm polystyrene beads (Fig. 6h). The MSD curves showed almost complete arrest of embedded particles in timescales on the order of 5 s (Fig. 6h), followed by a slow sub-diffusive motion (α ~ 0.86). This observation indicate that $[RGPGG]_5$-$(G4C2)_5$ condensates contain an elastic network which flows very slowly (τ_M > 5 sec). This behavior is opposite to $[RGPGG]_5$-dT40 condensates, which showed a linear MSD curve (α~0.99) without any detectable dynamical arrest of probe particles (Figs. 6h&2d). Based on these results, we conclude that the LVE properties of polypeptide-RNA condensates are strongly influenced by the RNA sequence composition, patterning, and secondary structure.

Discussion

Quantitative understanding of the molecular determinants of biomolecular condensates' dynamical properties is important for two reasons: (i) the knowledge of the condensate physical behavior at different time-scales (i.e., viscous *vs.* elastic regime) can provide invaluable insights into their functional regulation and their pathological liquid-to-solid transformation, and (ii) the establishment of a sequence-phase behavior-material property paradigm for disordered biopolymers akin to sequence-folding paradigm for globular proteins can enable building predictive models of biomolecular condensates and rational designing of synthetic membraneless organelles with programmable phase behavior and material properties. A growing number of recent studies indicate that biological condensates are viscoelastic fluids, and therefore exhibit distinct mechanical behavior at different timescales based on their network reconfiguration time (i.e., the making and breaking of physical crosslinks)[22,30,31,33]. Although, several theoretical works have attempted to quantitatively link the viscoelastic behavior of the condensates and the

molecular structure of their constituents[22,76-78], experimental studies on the same remain sparse due to limited suitable methods that can access the material properties within the minute volume of the condensed liquid phase. Recently, active oscillatory microrheology using a dual-trap optical tweezer[30,31] was used to explore protein condensate maturation over time. It was found that homotypic protein condensates age through slowing down of the dynamical motion within the condensates rather than increasing the elasticity of the condensates. Another recent work utilized similar methods to confirm the viscoelastic nature of biomolecular condensates and to point to the role of shear stress relaxation in controlling the condensate dynamics and fusion behavior[79]. The present study, however, focuses on linking the viscoelastic properties of polypeptide-RNA condensates to the sequence and structure of their constituent biopolymers by implementing passive microrheology with optical tweezers (pMOT). This is achieved through systematically exploring the frequency-dependent LVE properties of generic IDP-RNA condensates formed by RNP-inspired sticker-spacer polypeptides. Our results reveal that R/G-repeat polypeptide-RNA condensates resemble Maxwell fluids, which behave as an elastic solid at short timescales and a viscous fluid at long timescales. Both viscosity and the time-dependent network dynamics can be precisely controlled via polypeptide chain sequence, RNA sequence composition and secondary structure. These findings add significantly to the growing interest in characterizing and engineering rheological properties of biomolecular condensates by presenting a set of sequence analytics.

We speculate that the sequence heuristics obtained from our designer polypeptides can provide insights into the condensate network properties formed by RGG-domains of natural RNPs, which display a great deal of sequence and length variations. For example, the RGG-domains of FET proteins have diverse sequence features such as the occurrence of PGG motifs in EWSR1 and YGG motifs in TAF15 (Fig. S13a). Based on our results with synthetic condensates (Fig. 4a), we expected that EWSR1-RGG will have the fastest dynamics and least viscoelasticity due to the presence of multiple PGG motifs. Additionally, since TAF15-RGG has several YGG repeats as compared to FUS-RGG, we hypothesized that TAF15-RGG condensates will display stronger viscoelastic response than FUS-RGG. To test this idea, we measured the dynamical properties of condensates formed with representative RGG polypeptides from FUS, EWSR1, and TAF15 with a single-stranded nucleic acid (dT40), and observed that indeed $EWR1^{RGG}$ condensates display the most dynamic behavior (η~2 Pa.s, τ_M~20 ms) whereas $TAF15^{RGG}$ condensates are least dynamic (η~11 Pa.s, τ_M~300 ms; Fig. S13).

In addition to polypeptide sequence variations in a two component system, mixing multiple polypeptide chains with distinct sticker-spacer architectures, and/or RNA base composition and structure can also tune the LVE properties of condensates (Figs. 5&6), giving access to multiple routes of regulation. A rationalization of the observed variations in condensate dynamical properties comes from the consideration that inter-chain interactions dictate the thermodynamic and rheological properties of network fluids[29]. Using phase diagram analysis, diffusion measurements, and MD simulations, we found that the LVE properties of the dense phase are correlated with the relative strength of intermolecular interactions between the polypeptide and RNA chains. In our phase diagram analysis (Fig. 4c), we observed a strong correlation between the stability of condensates against salt and temperature and the linear viscoelasticity of the condensate network. Such a correlation can be understood using Flory-Huggins model of a phase separating mixture with UCST[61,62] (Fig. 6i). The mean-field intermolecular interactions between peptide-RNA complexes can be represented using the Flory parameter, χ. For simplicity, we consider two systems, A and B, with corresponding interaction parameters χ_A and χ_B ($\chi_A > \chi_B$;

Fig. 6i). Flory-Huggins theory predicts that UCST of system A will be higher than system B if $\chi_A > \chi_B$ and vice versa (Fig. 6i&4h). Therefore, at a common experimental temperature that is lower than the phase separation temperature of both systems, system A will be positioned at a larger quench depth (defined as the difference between the phase separation temperature and the experimental temperature) than system B (Fig. 6i). Without ruling out any other effects, the polymer density in the condensed phase of system A will be larger than the polymer density of system B in the dense phase. Polymer dynamics in the dense phase, including network relaxation time scales and the rheological properties, are often linked to polymer density and inter-chain bond relaxation times[77]. For example, complex coacervates formed by oppositely charged polymers were previously reported to exhibit slow Rouse-like relaxation modes that are described by a sticky Rouse polymer dynamics model[80]. In such a case, the viscosity of the condensate is proportional to the polymer density within the condensates. Moreover, the network relaxation dynamics are governed by the timescale of bond formation and breakage. We note that describing a multi-component peptide-RNA system solely in terms of a global Flory parameter (χ) is an oversimplification. Nevertheless, the particular choice of the model does not alter the drawn conclusions since most polymer UCST phase separation theories are generally consistent with the idea that stronger inter-chain attractions lead to denser condensed phases and that higher polymeric density leads to slower dynamics of the network structure due to steric forces and longer-lived physical bonds[61,81,82]. This explanation is consistent with our MD simulation results (Fig. 4d-h). Therefore, changing intermolecular interactions can regulate the rheological properties of the condensate through altering the polymer density within the condensed phase as well as the average bond lifetime (Fig. 6i).

In summary, our present work reports that the dynamical properties of a phase separated condensate depend on the nature and strength of inter-chain interactions. The material properties of biomolecular condensates are thought to be critical to their physiological function and arrested phase separation/ liquid-to-solid transitions have been linked to pathological dysfunction[19,83]. Laser tweezer-based microrheology of reconstituted RNP condensates can provide a deeper understanding of the context-dependent regulation of condensate material properties and enable the examination of various endogenous factors (such as post-translational modifications and genetic mutations) and exogenous effectors (small molecules) in manipulating their physical properties. Finally, engineered condensates formed by sticker-spacer polypeptides with programmable viscoelasticity can inspire new routes to design IDP-based soft biomaterials with tunable mechanics and provide a suitable platform to investigate how biochemical reaction dynamics are regulated by the condensate viscoelasticity.

DATA AVAILABILITY

All data relevant to the findings of this manuscript are included in the manuscript and the supplementary appendix. Additional data are available from the authors upon reasonable request.

CODE AVAILABILITY

All analysis and calculations were done using custom-made python scripts that are available upon reasonable request.

ACKNOWLEDGEMENTS

The authors acknowledge Dr. Manlio Tassieri of the University of Glasgow, UK for valuable discussions. P.R.B. acknowledges the College of Arts and Sciences at the University at Buffalo, SUNY, and the National Institute of General Medical Sciences (NIGMS) of the National Institutes of Health (R35 GM138186) for financial support. D.A.P acknowledges financial support from College of Liberal Arts and Sciences at the Iowa State University and the National Institute of General Medical Sciences (NIGMS) of the National Institutes of Health (R35 GM138243).

AUTHOR CONTRIBUTIONS

P.R.B. conceived the idea. P.R.B. and I.A. designed the study. I.A. performed the experiments and data analysis. M.M.M. performed the bioinformatics analysis. M.P. and D.A.P. performed all-atom and MD simulations. P.R.B. and I.A. wrote the manuscript with input from M.M.M. and D.A.P.

COMPETING INTERESTS

The authors declare no competing interests.

Figures and Legends

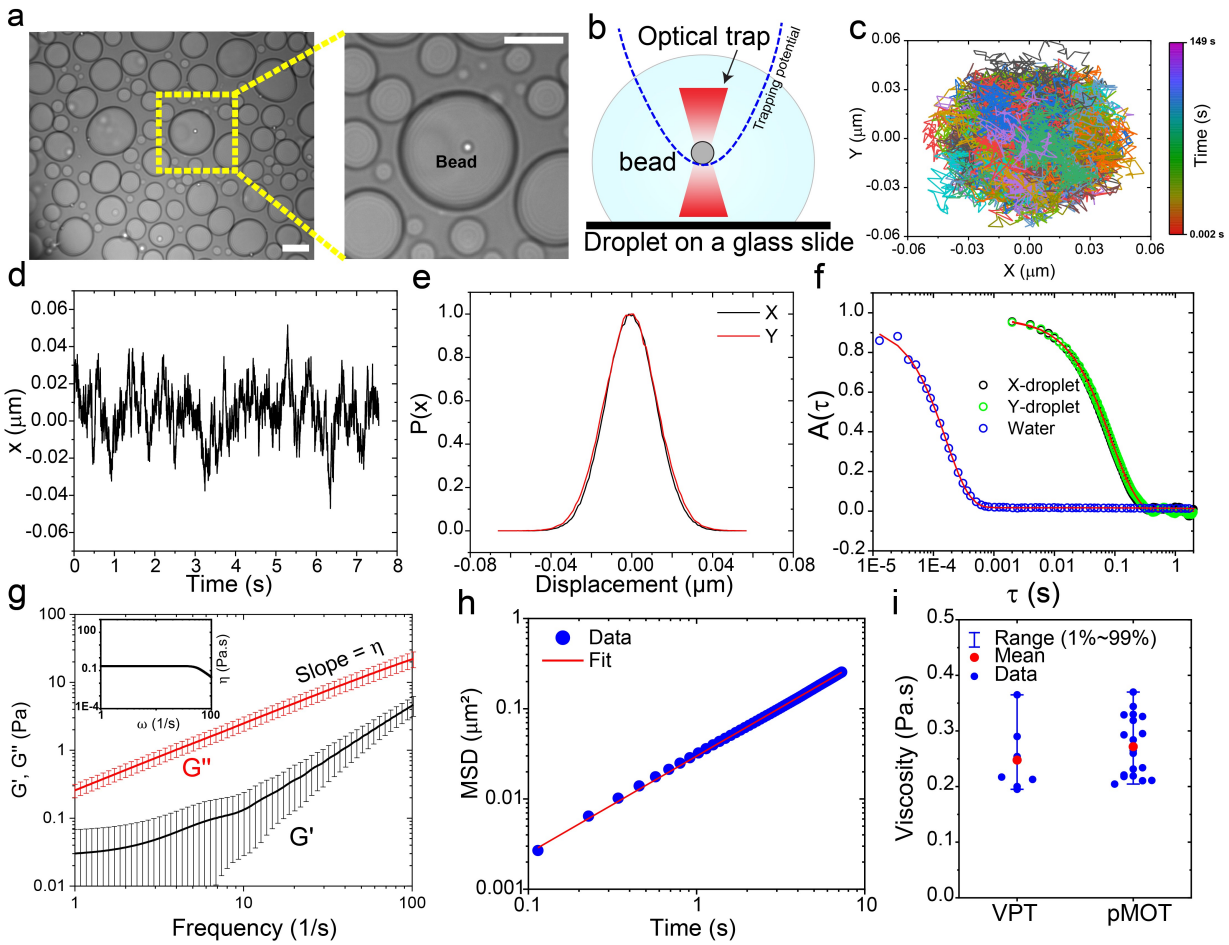

Figure 1. Determination of frequency-dependent viscoelastic moduli of peptide-RNA condensates using passive microrheology with optical tweezers (pMOT). (a) A bright-field image showing a polystyrene bead (1 μm) trapped within $[KGKGG]_5$-rU40 condensates using an optical trap. Scale bar = 10 μm. **(b)** A conceptual scheme of the pMOT experiment. The bead is optically trapped within a biomolecular condensate sitting on a microscope glass surface. **(c)** A representative 2D trajectory of the bead shown in (a) within the optical trap inside a $[KGKGG]_5$-rU40 condensate. **(d)** The trajectory of the trapped bead in the X-direction. **(e)** Normalized distribution of displacements along the X- and Y-directions for the trajectory in c&d. **(f)** The normalized position autocorrelation function [NPAF, A(t)] as calculated from the trajectory in (c) for a bead that is optically trapped inside $[KGKGG]_5$-rU40 condensate (green and black) and inside water (blue) as a reference. Solid lines are multi-exponential fits (see Supplementary Note 1). **(g)** The viscoelastic moduli as obtained from normalized position autocorrelation function using equation-1 for $[KGKGG]_5$-rU40 condensates. G' and G'' represent the elastic and viscous modulus, respectively. Solid lines are averages of the moduli of 10-20 condensates. Error bars represent the standard deviation as calculated from the moduli of 10-20 condensates. *Inset*: frequency-dependent condensate viscosity as determined from the viscous modulus using the relation $\eta(\omega) = G''(\omega)/\omega$. **(h)** The ensemble-averaged mean square displacement (MSD) of 200 nm polystyrene beads within $[KGKGG]_5$-rU40 condensates using video particle tracking (VPT)

microrheology in absence of optical traps (see Methods section for further details). **(i)** Comparison between the zero-shear viscosity as determined by pMOT and VPT-derived viscosity. Error bars represent the range of the data.

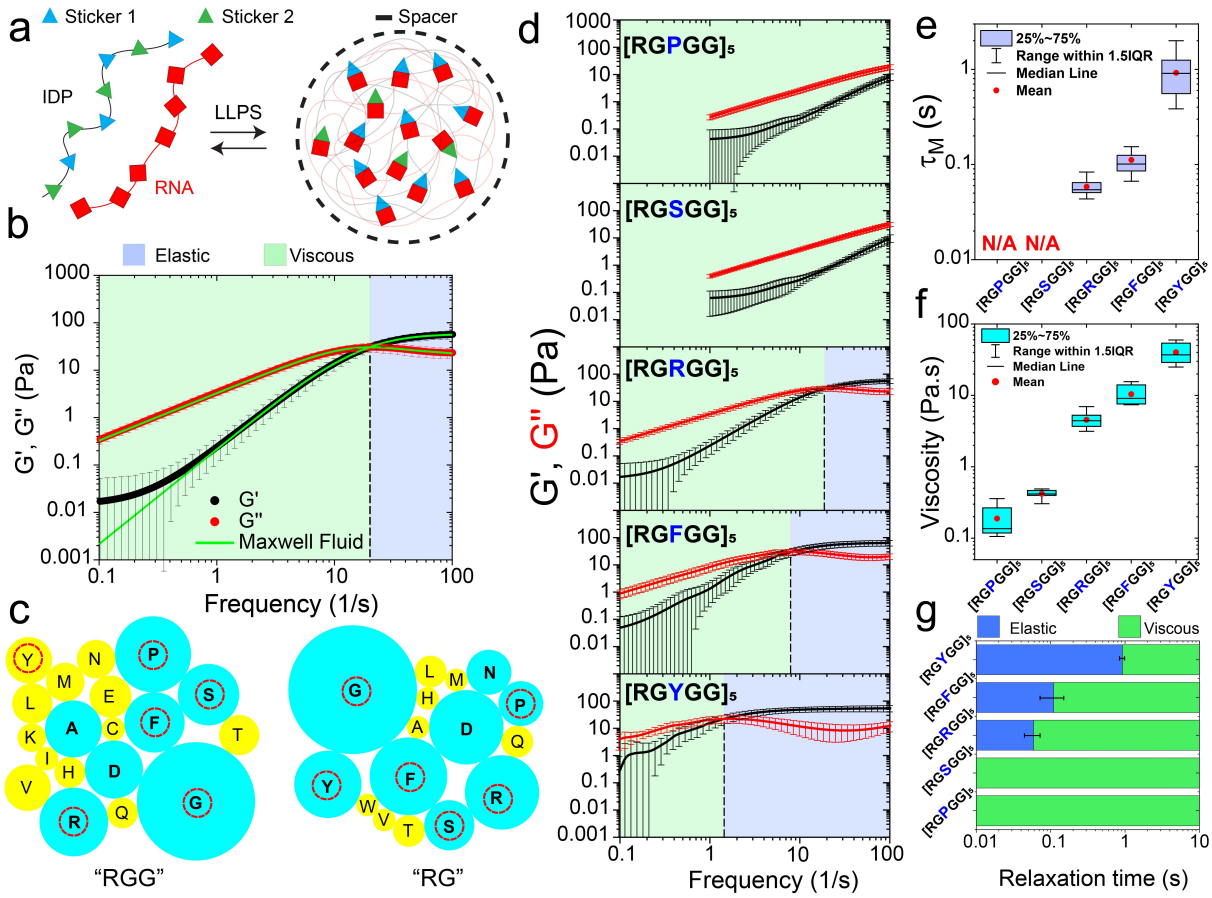

Figure 2. Sequence-dependent control over linear viscoelastic (LVE) behavior of peptide-RNA condensates. (a) A scheme showing the sticker-spacer architecture of associative peptide and RNA chains. Here, sticker-RNA interactions drive the condensation. **(b)** A plot showing the elastic modulus (G', black) and viscous modulus (G'', red) of $[RGRGG]_5$-rU40 condensates. Green lines are fits to experimental data using a single-mode Maxwell fluid model. The crossover frequency is indicated by the black dashed line and is the inverse of terminal relaxation time τ_M. Shaded regions represent the dominant elastic regime (light-blue) and the dominant viscous regime (light-green), respectively. Error bars represent one standard deviation (±1 s.d.). **(c)** The relative abundance of different amino acids within the inter-RG/RGG spacers of RG/RGG motifs in human RNA-binding proteins represented as bubble charts. Sizes of individual bubbles represent the fraction of inter-RG/RGG spacers that contain the corresponding amino acid (see Methods section). Residues that occurred in more than 10% of the analyzed protein sequences (RG/RGG domains from 407 human RNA-binding protein sequences) are indicated in cyan. Residues marked with red circles are utilized for peptide design for the experimental studies shown in this study. **(d)** Representative plots of the frequency-dependent viscoelastic moduli of $[RGXGG]_5$-rU40 condensates where X = P/S/R/F/Y. The crossover frequencies are indicated by black dashed lines. Shaded regions represent the dominant elastic regime (light-blue) and the dominant viscous regime (light-green), respectively. **(e)** The terminal relaxation time τ_M of $[RGXGG]_5$-rU40 condensates as measured by pMOT (X = P/S/R/F/Y). **(f)** The zero-shear viscosity of $[RGXGG]_5$-rU40 condensates as measured by pMOT (X = P/S/R/F/Y). **(g)** An LVE state diagram indicating the timescales at which the elastic modulus dominates (blue) and the

timescales where the viscous modulus dominates (green) in [RG<u>X</u>GG]$_5$-rU40 condensates (X = P/S/R/F/Y).

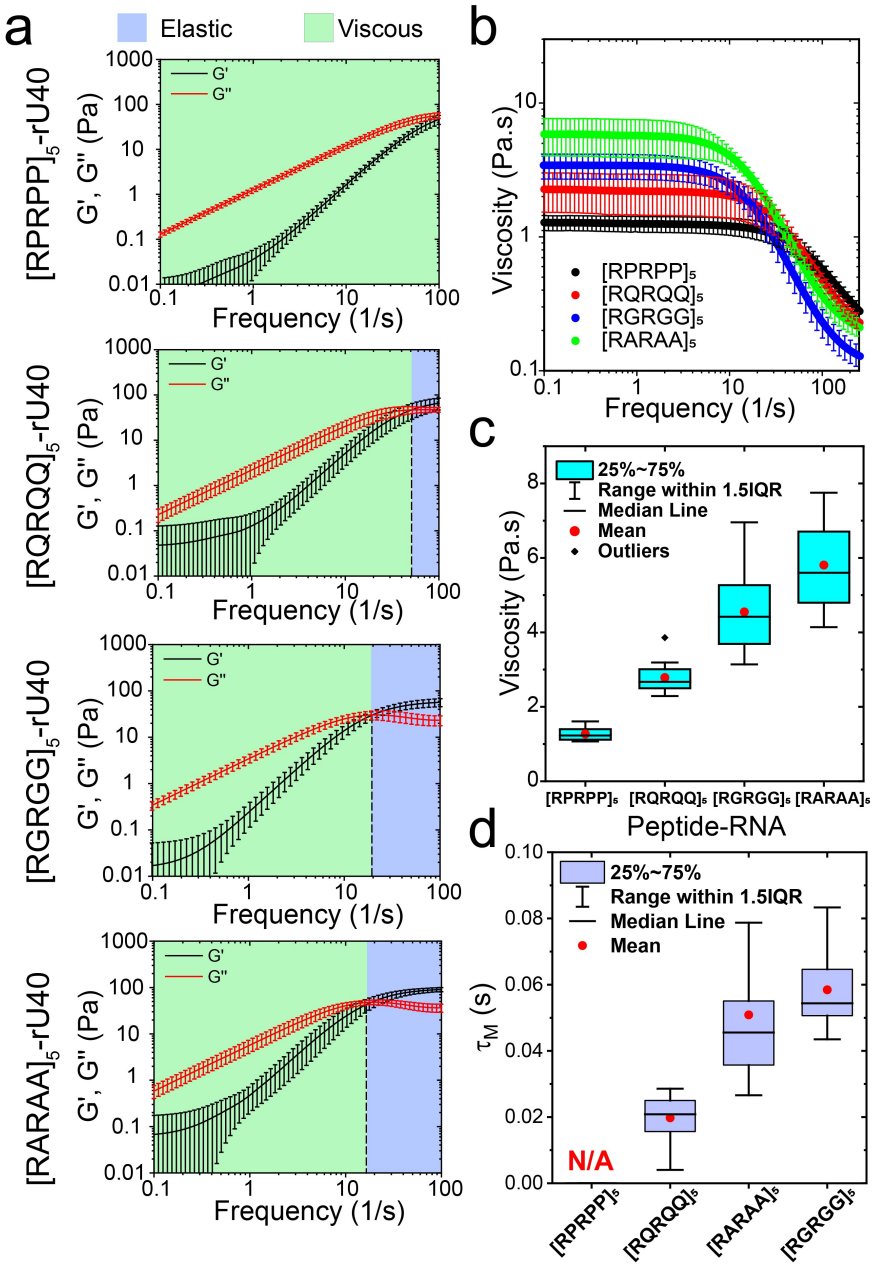

Figure 3. Effect of spacer sequence variation on the frequency-dependent viscoelasticity of peptide-RNA condensates. (a) Viscoelastic moduli of [RxRxx]$_5$-rU40 condensates. The crossover frequencies are indicated by black dashed lines. Shaded regions represent the dominant elastic regime (light-blue) and the dominant viscous regime (light-green), respectively. Error bars represent one standard deviation (±1 s.d.). **(b)** The frequency-dependent viscosity of [RxRxx]$_5$-rU40 condensates as measured by pMOT. **(c)** The zero-shear viscosity of [RxRxx]$_5$-rU40 condensates as measured by pMOT. **(d)** The terminal relaxation time τ_M of [RxRxx]$_5$-rU40 condensates as measured by pMOT. For data shown in (a)-(d): x = P/Q/G/A.

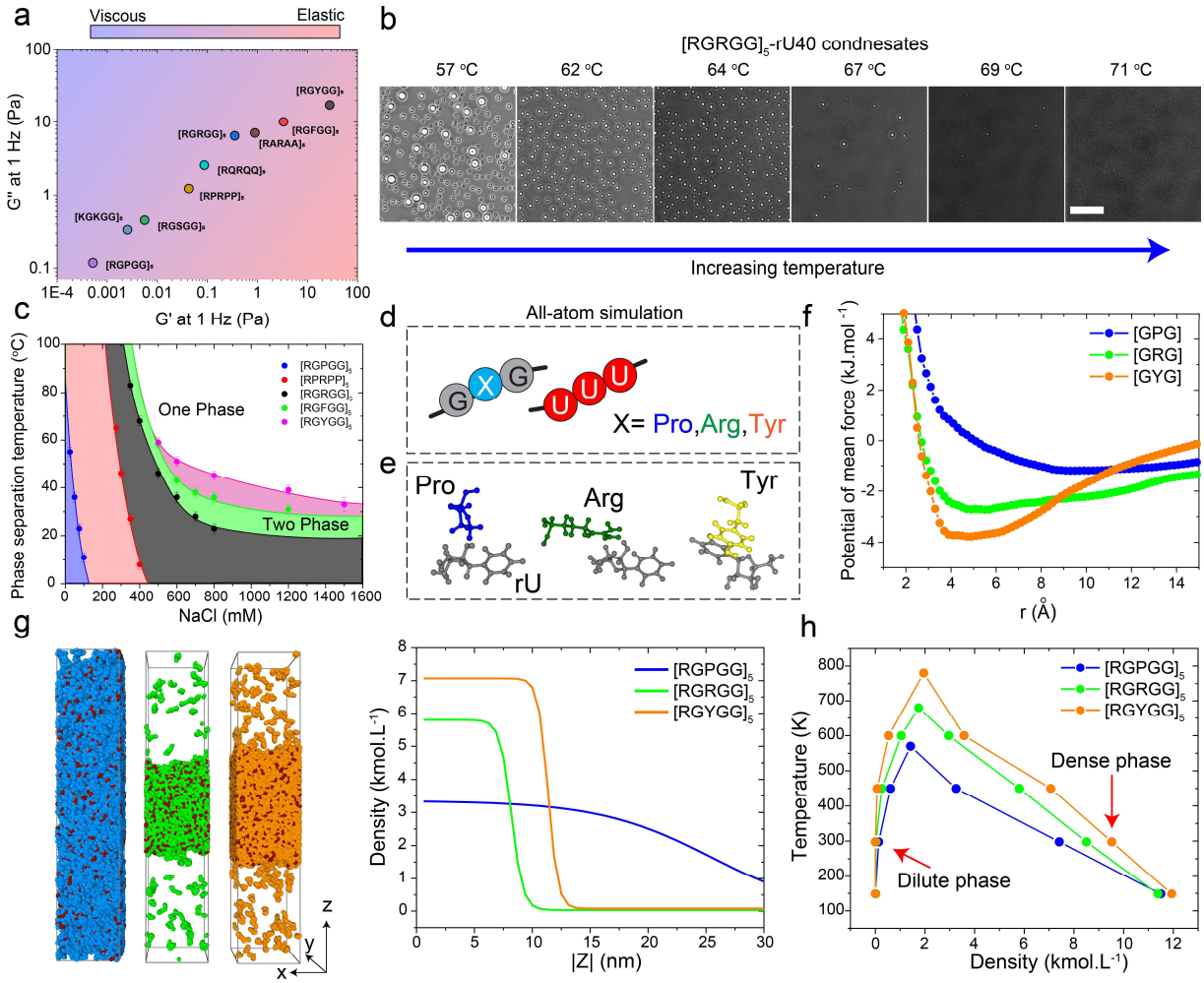

Figure 4. Peptide-RNA interactions govern the condensate LVE properties. (a) A material state diagram showing the elastic (G') and viscous (G'') moduli at 1 Hz frequency for the various condensates tested in this study. This plot shows a broad range of tunability in condensate viscoelasticity via sequence perturbations. **(b)** Bright-field images of $[RGRGG]_5$-rU40 condensates showing phase separation upon cooling. Scale bar is 20 µm. **(c)** Temperature-salt state diagram for $[RGPGG]_5$, $[RPRPP]_5$, $[RGRGG]_5$, $[RGFGG]_5$, and $[RGYGG]_5$ mixtures with rU40 RNA. Shaded regions indicate the salt and temperature conditions that allow phase separation. The most stable peptide-RNA condensates are $[RGYGG]_5$-rU40 and the least stable are $[RGPGG]_5$-rU40 condensates. Error bars represent the temperature range between a phase separated sample and a homogeneous (not phase separated) sample. **(d)** A scheme summarizing the all-atom simulations of tri-amino acids [GXG] and a tri-nucleotide [rUrUrU] where X was set to either Arg or Pro or Tyr. **(e)** All-atom simulation equilibrium snapshots of Pro-rU, Arg-rU and Tyr-rU interactions. Note the π-π stacking in the case of Tyr-rU pair that leads to stronger interactions with RNA. **(f)** Free energy profiles of [GXG]-[rUrUrU] attraction from model peptide-RNA all-atom constant temperature simulations shown in (e). X is set to Arg, Pro, and Tyr. The tripeptide that is stickiest to [rUrUrU] is [GYG] while [GPG] has the weakest interaction with the trinucleotide. **(g)** Snapshots from the coexistence simulations with coarse grained molecular models of full peptide sequences and rU40 RNA showing the equilibrium configuration of peptide and RNA chains in $[RGPGG]_5$-rU40, $[RGRGG]_5$-rU40, and $[RGYGG]_5$-rU40 mixtures at a

temperature of 450K. The rU units are colored in red. The Pro units are colored in blue. The Arg units are colored in green. The Tyr units are colored in orange. Corresponding density profiles are shown along the z-direction of the box. **(h)** Temperature-density phase diagrams for $[RGPGG]_5$-rU40, $[RGRGG]_5$-rU40, and $[RGYGG]_5$-rU40 condensates as extracted from the coexistence simulations in (g). At each temperature, the densities of the condensed and dilute phases are shown.

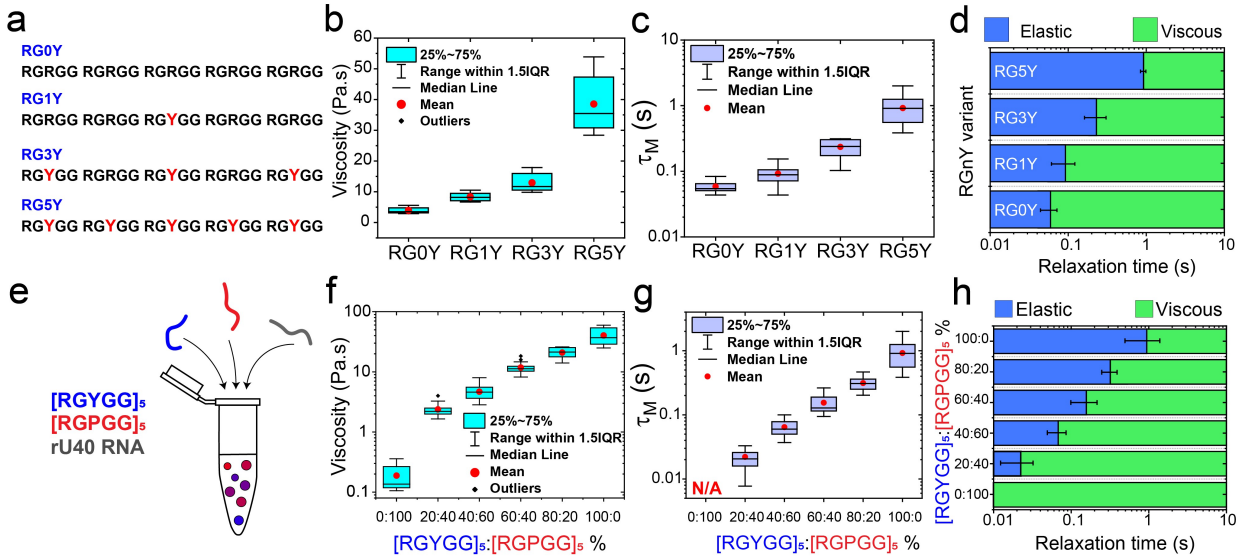

Figure 5. Continuous tuning of LVE behavior of peptide-RNA condensates by two orthogonal approaches. (a) Polypeptide sequences of the RGnY peptide design with n representing the number of Tyr residues. RG0Y corresponds to $[RGRGG]_5$, RG5Ycorresponds to $[RGYGG]_5$ (see Table S1). **(b)** The zero-shear viscosity of RGnY-rU40 condensates as measured by pMOT. **(c)** The terminal relaxation time τ_M of RGnY-rU40 condensates as measured by pMOT (see Fig. S10). **(d)** An experimental LVE state diagram indicating the timescales at which the elastic modulus dominates (blue) and the time scales where the viscous modulus dominates (green) in RGnY-rU40 condensates. **(e)** A scheme showing the preparation of condensates formed by mixing $[RGYGG]_5$, $[RGPGG]_5$, and rU40 RNA with variable $[RGYGG]_5$-to-$[RGPGG]_5$ ratios. Here, the total peptide concentration is fixed at 5.0 mg/ml and the relative fractions of $[RGYGG]_5$ and $[RGPGG]_5$ are varied. **(f)** The zero-shear viscosity of condensates formed by mixtures of $[RGYGG]_5$, $[RGPGG]_5$, and RNA at variable $[RGYGG]_5$-to-$[RGPGG]_5$ ratios. **(g)** The terminal relaxation time (τ_M) of the same condensates as in (f). See Fig. S12 for the viscoelastic moduli. **(h)** An experimental LVE state diagram indicating the timescales at which the elastic modulus dominates (blue) and the timescales where the viscous modulus dominates (green) in $[RGYGG]_5$-$[RGPGG]_5$-rU40 condensates as a function of $[RGYGG]_5$-to-$[RGPGG]_5$ ratio.

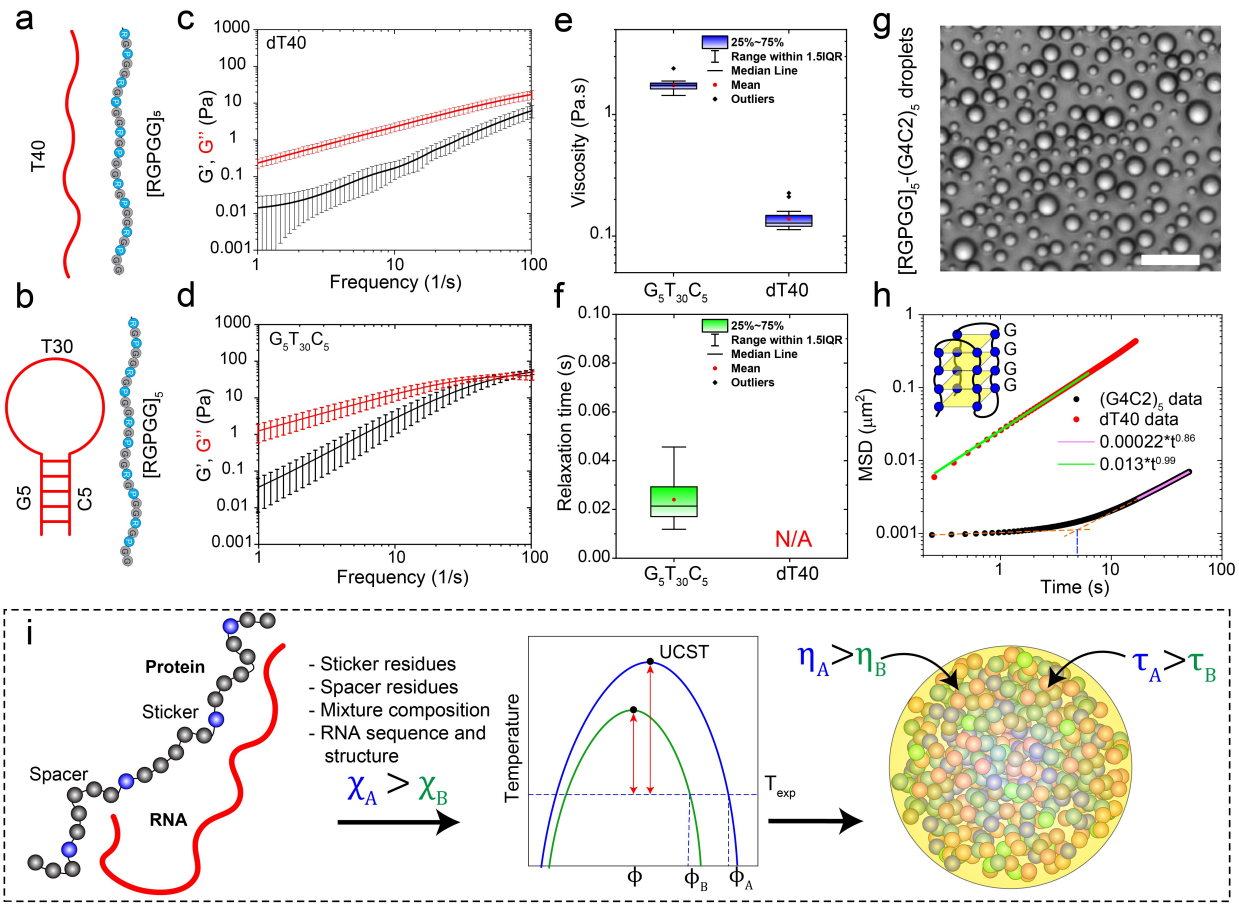

Figure 6. Effect of RNA sequence and structure on the LVE properties of peptide-RNA condensates. (a) A scheme showing the sequence and expected structure of the peptide and dT40. **(b)** A Scheme showing the sequence and structure of $G_5T_{30}C_5$. **(c)** Viscoelastic moduli of condensates formed by $[RGPGG]_5$ and dT40 as measured by pMOT. **(d)** Viscoelastic moduli of condensates formed by $[RGPGG]_5$ and $G_5T_{30}C_5$ as measured by pMOT. **(e)** Zero-shear viscosity of $[RGPGG]_5$-ssNA condensates for both structured ($G_5T_{30}C_5$) and unstructured (dT40) NA as calculated from the data in (b) & (d). **(f)** Terminal relaxation time of $[RGPGG]_5$-NA condensates for both structured ($G_5T_{30}C_5$) and unstructured (dT40) NA as calculated from the data in (b) & (d). **(g)** Brightfield image of condensates prepared by mixing $[RGPGG]_5$ and $(G_4C_2)_5$ NA at 5.0 mg/ml and 2.5 mg/ml concentrations, respectively. Scale bar is 20 μm. **(h)** Mean squared displacement (MSD) of 200 nm polystyrene particles within condensates formed by $[RGPGG]_5$ peptide with dT40 (red) and $(G_4C_2)_5$ (black). This data show that $(G_4C_2)_5$ forms condensates that have substantially slower network dynamics as compared to the condensates formed by dT40. The orange dashed lines extrapolate the two behaviors (flat MSD at short lag-times and increasing MSD at long lag-times) and the blue line indicates the extrapolated transition point at ~5 s. **(i)** A scheme summarizing the relation between the strength of intermolecular interactions and LVE properties of peptide-RNA condensates. Comparison between two idealized systems A (blue) and B (green) is shown with $\chi_A > \chi_B$. Due to stronger interactions in system A, the difference between the phase separation temperature (blue curve) and the experimental temperature is greater, leading to a deeper quench within the two-phase regime (red double-sided arrow).

Additionally, stronger interactions in system A cause higher viscosity η and a slower bond reconfiguration time τ, which retards the network flow.

References

1 Iserman, C. *et al.* Genomic RNA elements drive phase separation of the SARS-CoV-2 nucleocapsid. *Molecular cell* **80**, 1078-1091. e1076 (2020).

2 Azaldegui, C. A., Vecchiarelli, A. G. & Biteen, J. S. The emergence of phase separation as an organizing principle in bacteria. *Biophysical journal* **120**, 1123-1138 (2021).

3 Ladouceur, A.-M. *et al.* Clusters of bacterial RNA polymerase are biomolecular condensates that assemble through liquid–liquid phase separation. *Proceedings of the National Academy of Sciences* **117**, 18540-18549 (2020).

4 Franzmann, T. M. *et al.* Phase separation of a yeast prion protein promotes cellular fitness. *Science* **359** (2018).

5 Laflamme, G. & Mekhail, K. Biomolecular condensates as arbiters of biochemical reactions inside the nucleus. *Communications Biology* **3**, 1-8 (2020).

6 Lyon, A. S., Peeples, W. B. & Rosen, M. K. A framework for understanding the functions of biomolecular condensates across scales. *Nature Reviews Molecular Cell Biology*, 1-21 (2020).

7 Molliex, A. *et al.* Phase separation by low complexity domains promotes stress granule assembly and drives pathological fibrillization. *Cell* **163**, 123-133 (2015).

8 Guillén-Boixet, J. *et al.* RNA-induced conformational switching and clustering of G3BP drive stress granule assembly by condensation. *Cell* **181**, 346-361. e317 (2020).

9 Fay, M. M. & Anderson, P. J. The role of RNA in biological phase separations. *Journal of molecular biology* **430**, 4685-4701 (2018).

10 Boija, A. *et al.* Transcription factors activate genes through the phase-separation capacity of their activation domains. *Cell* **175**, 1842-1855. e1816 (2018).

11 Hnisz, D., Shrinivas, K., Young, R. A., Chakraborty, A. K. & Sharp, P. A. A phase separation model for transcriptional control. *Cell* **169**, 13-23 (2017).

12 Sabari, B. R. *et al.* Coactivator condensation at super-enhancers links phase separation and gene control. *Science* **361** (2018).

13 Gibson, B. A. *et al.* Organization of chromatin by intrinsic and regulated phase separation. *Cell* **179**, 470-484. e421 (2019).

14 Patel, A. *et al.* A Liquid-to-Solid Phase Transition of the ALS Protein FUS Accelerated by Disease Mutation. *Cell* **162**, 1066-1077, doi:https://doi.org/10.1016/j.cell.2015.07.047 (2015).

15 St George-Hyslop, P. *et al.* The physiological and pathological biophysics of phase separation and gelation of RNA binding proteins in amyotrophic lateral sclerosis and fronto-temporal lobar degeneration. *Brain research* **1693**, 11-23 (2018).

16 Murakami, T. *et al.* ALS/FTD mutation-induced phase transition of FUS liquid droplets and reversible hydrogels into irreversible hydrogels impairs RNP granule function. *Neuron* **88**, 678-690 (2015).

17 Nair, S. J. *et al.* Phase separation of ligand-activated enhancers licenses cooperative chromosomal enhancer assembly. *Nature Structural & Molecular Biology* **26**, 193-203, doi:10.1038/s41594-019-0190-5 (2019).

18 Risso-Ballester, J. *et al.* A condensate-hardening drug blocks RSV replication in vivo. *Nature*, 1-4 (2021).

19 Mathieu, C., Pappu, R. V. & Taylor, J. P. Beyond aggregation: Pathological phase transitions in neurodegenerative disease. *Science* **370**, 56-60 (2020).

20 Li, W. *et al.* Biophysical properties of AKAP95 protein condensates regulate splicing and tumorigenesis. *Nature cell biology* **22**, 960-972 (2020).

21 Woodruff, J. B., Hyman, A. A. & Boke, E. Organization and function of non-dynamic biomolecular condensates. *Trends in biochemical sciences* **43**, 81-94 (2018).
22 Choi, J.-M., Holehouse, A. S. & Pappu, R. V. Physical principles underlying the complex biology of intracellular phase transitions. *Annual Review of Biophysics* **49** (2020).
23 Shin, Y. & Brangwynne, C. P. Liquid phase condensation in cell physiology and disease. *Science* **357**, eaaf4382 (2017).
24 Semenov, A. N. & Rubinstein, M. Thermoreversible Gelation in Solutions of Associative Polymers. 1. Statics. *Macromolecules* **31**, 1373-1385, doi:10.1021/ma970616h (1998).
25 Choi, J.-M., Dar, F. & Pappu, R. V. LASSI: A lattice model for simulating phase transitions of multivalent proteins. *PLoS computational biology* **15** (2019).
26 Harmon, T. S., Holehouse, A. S., Rosen, M. K. & Pappu, R. V. Intrinsically disordered linkers determine the interplay between phase separation and gelation in multivalent proteins. *elife* **6**, e30294 (2017).
27 Martin, E. W. *et al.* Valence and patterning of aromatic residues determine the phase behavior of prion-like domains. *Science* **367**, 694-699 (2020).
28 Bremer, A. *et al.* Deciphering how naturally occurring sequence features impact the phase behaviors of disordered prion-like domains. *bioRxiv*, 2021.2001.2001.425046, doi:10.1101/2021.01.01.425046 (2021).
29 Dias, C., Araújo, N. & da Gama, M. T. Dynamics of network fluids. *Advances in colloid and interface science* **247**, 258-263 (2017).
30 Jawerth, L. M. *et al.* Salt-dependent rheology and surface tension of protein condensates using optical traps. *Physical review letters* **121**, 258101 (2018).
31 Jawerth, L. *et al.* Protein condensates as aging Maxwell fluids. *Science* **370**, 1317-1323 (2020).
32 Espinosa, J. R. *et al.* Liquid network connectivity regulates the stability and composition of biomolecular condensates with many components. *Proceedings of the National Academy of Sciences* **117**, 13238-13247 (2020).
33 Feric, M. *et al.* Coexisting liquid phases underlie nucleolar subcompartments. *Cell* **165**, 1686-1697 (2016).
34 Rubinstein, M. & Colby, R. H. *Polymer physics*. Vol. 23 (Oxford university press New York, 2003).
35 Mason, T. G. & Weitz, D. A. Optical measurements of frequency-dependent linear viscoelastic moduli of complex fluids. *Physical review letters* **74**, 1250 (1995).
36 Brau, R. *et al.* Passive and active microrheology with optical tweezers. *Journal of Optics A: Pure and Applied Optics* **9**, S103 (2007).
37 Tassieri, M. *Microrheology with Optical Tweezers: Principles and Applications*. (CRC Press, 2016).
38 Preece, D. *et al.* Optical tweezers: wideband microrheology. *Journal of optics* **13**, 044022 (2011).
39 Tassieri, M., Evans, R., Warren, R. L., Bailey, N. J. & Cooper, J. M. Microrheology with optical tweezers: data analysis. *New Journal of Physics* **14**, 115032 (2012).
40 Tassieri, M. *et al.* Measuring storage and loss moduli using optical tweezers: Broadband microrheology. *Physical Review E* **81**, 026308 (2010).
41 Alshareedah, I., Thurston, G. M. & Banerjee, P. R. Quantifying Viscosity and Surface Tension of Multi-Component Protein-Nucleic Acid Condensates. *Biophysical journal*, doi:https://doi.org/10.1016/j.bpj.2021.01.005 (2021).
42 Alshareedah, I., Moosa, M. M., Raju, M., Potoyan, D. A. & Banerjee, P. R. Phase transition of RNA−protein complexes into ordered hollow condensates. *Proceedings of the National Academy of Sciences* **117**, 15650-15658, doi:10.1073/pnas.1922365117 (2020).

43 Banerjee, P. R., Milin, A. N., Moosa, M. M., Onuchic, P. L. & Deniz, A. A. Reentrant phase transition drives dynamic substructure formation in ribonucleoprotein droplets. *Angewandte Chemie International Edition* **56**, 11354-11359 (2017).
44 Alshareedah, I. *et al.* Interplay between Short-Range Attraction and Long-Range Repulsion Controls Reentrant Liquid Condensation of Ribonucleoprotein–RNA Complexes. *Journal of the American Chemical Society* **141**, 14593-14602, doi:10.1021/jacs.9b03689 (2019).
45 Fisher, R. S. & Elbaum-Garfinkle, S. Tunable multiphase dynamics of arginine and lysine liquid condensates. *Nature communications* **11**, 1-10 (2020).
46 Zhang, H. *et al.* RNA controls PolyQ protein phase transitions. *Molecular cell* **60**, 220-230 (2015).
47 Boeynaems, S. *et al.* Phase separation of C9orf72 dipeptide repeats perturbs stress granule dynamics. *Molecular cell* **65**, 1044-1055. e1045 (2017).
48 Boeynaems, S. *et al.* Spontaneous driving forces give rise to protein− RNA condensates with coexisting phases and complex material properties. *Proceedings of the National Academy of Sciences* **116**, 7889-7898 (2019).
49 Chong, P. A., Vernon, R. M. & Forman-Kay, J. D. RGG/RG motif regions in RNA binding and phase separation. *Journal of molecular biology* **430**, 4650-4665 (2018).
50 Aumiller, W. M. & Keating, C. D. Phosphorylation-mediated RNA/peptide complex coacervation as a model for intracellular liquid organelles. *Nature chemistry* **8**, 129-137 (2016).
51 Ozdilek, B. A. *et al.* Intrinsically disordered RGG/RG domains mediate degenerate specificity in RNA binding. *Nucleic acids research* **45**, 7984-7996 (2017).
52 Thandapani, P., O'Connor, T. R., Bailey, T. L. & Richard, S. Defining the RGG/RG motif. *Molecular cell* **50**, 613-623 (2013).
53 Greig, J. A. *et al.* Arginine-enriched mixed-charge domains provide cohesion for nuclear speckle condensation. *Molecular Cell* (2020).
54 Cook, K. B., Kazan, H., Zuberi, K., Morris, Q. & Hughes, T. R. RBPDB: a database of RNA-binding specificities. *Nucleic acids research* **39**, D301-D308 (2010).
55 Chaudhuri, O., Cooper-White, J., Janmey, P. A., Mooney, D. J. & Shenoy, V. B. Effects of extracellular matrix viscoelasticity on cellular behaviour. *Nature* **584**, 535-546 (2020).
56 Kee, H. L. *et al.* A size-exclusion permeability barrier and nucleoporins characterize a ciliary pore complex that regulates transport into cilia. *Nature cell biology* **14**, 431-437 (2012).
57 Wei, M.-T. *et al.* Phase behaviour of disordered proteins underlying low density and high permeability of liquid organelles. *Nature chemistry* **9**, 1118-1125 (2017).
58 Vernon, R. M. *et al.* Pi-Pi contacts are an overlooked protein feature relevant to phase separation. *elife* **7**, e31486 (2018).
59 Ruff, K. M., Roberts, S., Chilkoti, A. & Pappu, R. V. Advances in understanding stimulus-responsive phase behavior of intrinsically disordered protein polymers. *Journal of molecular biology* **430**, 4619-4635 (2018).
60 Dignon, G. L., Zheng, W., Kim, Y. C. & Mittal, J. Temperature-controlled liquid–liquid phase separation of disordered proteins. *ACS central science* **5**, 821-830 (2019).
61 Flory, P. J. Thermodynamics of high polymer solutions. *The Journal of chemical physics* **10**, 51-61 (1942).
62 Huggins, M. L. Some properties of solutions of long-chain compounds. *The Journal of Physical Chemistry* **46**, 151-158 (1942).
63 Tainaka, K.-i. Study of complex coacervation in low concentration by virial expansion method. I. Salt free systems. *Journal of the Physical Society of Japan* **46**, 1899-1906 (1979).

64 Robustelli, P., Piana, S. & Shaw, D. E. Developing a molecular dynamics force field for both folded and disordered protein states. *Proceedings of the National Academy of Sciences* **115**, E4758-E4766 (2018).
65 de Ruiter, A. & Zagrovic, B. Absolute binding-free energies between standard RNA/DNA nucleobases and amino-acid sidechain analogs in different environments. *Nucleic acids research* **43**, 708-718 (2015).
66 Kaur, T. *et al.* Sequence-encoded and composition-dependent protein-RNA interactions control multiphasic condensate morphologies. *Nature communications* **12**, 1-16 (2021).
67 Simon, J. R., Carroll, N. J., Rubinstein, M., Chilkoti, A. & López, G. P. Programming molecular self-assembly of intrinsically disordered proteins containing sequences of low complexity. *Nature chemistry* **9**, 509 (2017).
68 Roden, C. & Gladfelter, A. S. RNA contributions to the form and function of biomolecular condensates. *Nature Reviews Molecular Cell Biology* **22**, 183-195 (2021).
69 Merindol, R., Loescher, S., Samanta, A. & Walther, A. Pathway-controlled formation of mesostructured all-DNA colloids and superstructures. *Nature nanotechnology* **13**, 730-738 (2018).
70 Biot, C., Buisine, E., Kwasigroch, J.-M., Wintjens, R. & Rooman, M. Probing the energetic and structural role of amino acid/nucleobase cation-π interactions in protein-ligand complexes. *Journal of Biological Chemistry* **277**, 40816-40822 (2002).
71 Zhou, B., Liu, C., Geng, Y. & Zhu, G. Topology of a G-quadruplex DNA formed by C9orf72 hexanucleotide repeats associated with ALS and FTD. *Scientific reports* **5**, 1-7 (2015).
72 DeJesus-Hernandez, M. *et al.* Expanded GGGGCC hexanucleotide repeat in noncoding region of C9ORF72 causes chromosome 9p-linked FTD and ALS. *Neuron* **72**, 245-256 (2011).
73 Takahama, K. & Oyoshi, T. Specific binding of modified RGG domain in TLS/FUS to G-quadruplex RNA: tyrosines in RGG domain recognize 2′-OH of the riboses of loops in G-quadruplex. *Journal of the American Chemical Society* **135**, 18016-18019 (2013).
74 Ghosh, M. & Singh, M. RGG-box in hnRNPA1 specifically recognizes the telomere G-quadruplex DNA and enhances the G-quadruplex unfolding ability of UP1 domain. *Nucleic acids research* **46**, 10246-10261 (2018).
75 Huang, Z.-L. *et al.* Identification of G-quadruplex-binding protein from the exploration of RGG motif/G-quadruplex interactions. *Journal of the American Chemical Society* **140**, 17945-17955 (2018).
76 Rubinstein, M. & Semenov, A. N. Thermoreversible gelation in solutions of associating polymers. 2. Linear dynamics. *Macromolecules* **31**, 1386-1397 (1998).
77 Rubinstein, M. & Semenov, A. N. Dynamics of entangled solutions of associating polymers. *Macromolecules* **34**, 1058-1068 (2001).
78 Rubinstein, M. & Dobrynin, A. V. Associations leading to formation of reversible networks and gels. *Current opinion in colloid & interface science* **4**, 83-87 (1999).
79 Ghosh, A., Kota, D. & Zhou, H.-X. Shear Relaxation Governs Dynamic Processes of Biomolecular Condensates. *bioRxiv* (2021).
80 Spruijt, E., Cohen Stuart, M. A. & van der Gucht, J. Linear viscoelasticity of polyelectrolyte complex coacervates. *Macromolecules* **46**, 1633-1641 (2013).
81 Lin, Y.-H., Song, J., Forman-Kay, J. D. & Chan, H. S. Random-phase-approximation theory for sequence-dependent, biologically functional liquid-liquid phase separation of intrinsically disordered proteins. *Journal of Molecular Liquids* **228**, 176-193 (2017).
82 Overbeek, J. T. G. & Voorn, M. Phase separation in polyelectrolyte solutions. Theory of complex coacervation. *Journal of Cellular and Comparative Physiology* **49**, 7-26 (1957).
83 Forman-Kay, J. D., Kriwacki, R. W. & Seydoux, G. Phase separation in biology and disease. *Journal of molecular biology* **430**, 4603 (2018).